Nano-Micro Letters

e-ISSN 2150-5551
CN 31-2103/TB

ARTICLE

https://doi.org/10.1007/s40820-022-00884-8

Check for updates

Cite as
Nano-Micro Lett.
(2022) 14:164

Received: 16 March 2022
Accepted: 24 May 2022

Effects of Flexible Conjugation-Break Spacers of Non-Conjugated Polymer Acceptors on Photovoltaic and Mechanical Properties of All-Polymer Solar Cells

Qiaonan Chen[1,2], Yung Hee Han[3], Leandro R. Franco[4], Cleber F. N. Marchiori[4], Zewdneh Genene[2], C. Moyses Araujo[4,7], Jin-Woo Lee[3], Tan Ngoc-Lan Phan[3], Jingnan Wu[2,5], Donghong Yu[5,8], Dong Jun Kim[6], Taek-Soo Kim[6], Lintao Hou[1] ✉, Bumjoon J. Kim[3] ✉, Ergang Wang[2,9] ✉

HIGHLIGHTS

- A series of non-conjugated acceptor polymers with flexible conjugation-break spacers (FCBSs) of different lengths were synthesized.
- The effect of FCBSs length on solubility of the acceptor polymers, and their photovoltaic and mechanical properties in all-polymer solar cells were explored.
- This work provides useful guidelines for the design of semiconducting polymers by introducing FCBS with proper length, which can giantly improved properties that are not possible to be achieved by the state-of-the-art fully conjugated polymers.

ABSTRACT All-polymer solar cells (all-PSCs) possess attractive merits including superior thermal stability and mechanical flexibility for large-area roll-to-roll processing. Introducing flexible conjugation-break spacers (FCBSs) into backbones of polymer donor (P_D) or polymer acceptor (P_A) has been demonstrated as an efficient approach to enhance both the photovoltaic (PV) and mechanical properties of the all-PSCs. However, length dependency of FCBS on certain all-PSC related properties has not been systematically explored. In this regard, we report a series of new non-conjugated P_As by incorporating FCBS with various lengths (2, 4, and 8 carbon atoms in thioalkyl segments). Unlike common studies on so-called side-chain engineering, where longer side chains would lead to better solubility of those resulting polymers, in this work, we observe that the solubilities and the resulting photovoltaic/mechanical properties are optimized by a proper FCBS length (*i.e.*, C2) in P_A named PYTS-C2. Its all-PSC achieves a high efficiency of 11.37%, and excellent mechanical robustness with a crack onset strain of 12.39%, significantly superior to those of the other P_As. These results firstly demonstrate the effects of FCBS lengths on the PV performance and mechanical properties of the all-PSCs, providing an effective strategy to fine-tune the structures of P_As for highly efficient and mechanically robust PSCs.

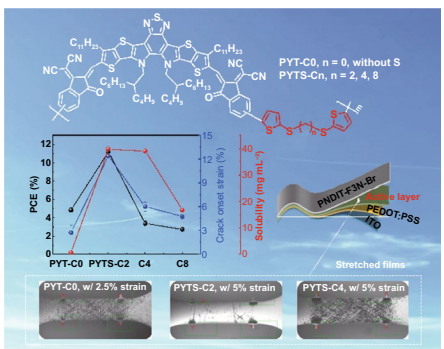

KEYWORDS All-polymer solar cells; Flexible conjugation-break spacers; Mechanical robustness; Polymer acceptors; Stretchability

Qiaonan Chen and Yung Hee Han have contributed equally to this work.

✉ Lintao Hou, thlt@jnu.edu.cn; Bumjoon J. Kim, bumjoonkim@kaist.ac.kr; Ergang Wang, ergang@chalmers.se

[1] Siyuan Laboratory, Guangzhou Key Laboratory of Vacuum Coating Technologies and New Energy Materials, Department of Physics, Jinan University, Guangzhou 510632, People's Republic of China
[2] Department of Chemistry and Chemical Engineering, Chalmers University of Technology, SE-412 96, Göteborg, Sweden
[3] Department of Chemical and Biomolecular Engineering, Korea Advanced Institute of Science and Technology (KAIST), Daejeon 34141, Republic of Korea
[4] Department of Engineering and Physics, Karlstad University, 65188 Karlstad, Sweden
[5] Department of Chemistry and Bioscience, Aalborg University, 9220 Aalborg, Denmark
[6] Department of Mechanical Engineering, Korea Advanced Institute of Science and Technology (KAIST), Daejeon 34141, Republic of Korea
[7] Materials Theory Division, Department of Physics and Astronomy, Uppsala University, 75120 Uppsala, Sweden
[8] Sino-Danish Center for Education and Research, 8000 Aarhus, Denmark
[9] School of Materials Science and Engineering, Zhengzhou University, Zhengzhou 450001, People's Republic of China

Published online: 13 August 2022

Shanghai Jiao Tong University Press

Springer

1 Introduction

Polymer solar cells (PSCs) have attracted extensive research attention due to their straight advantages of light-weight, flexibility, transparency, low cost, and facile large-area fabrication [1–5]. Driven by those benefits, non-fullerene PSCs based on tailor-made polymer donors (P_Ds) and continually developing fused-ring small molecular acceptors (SMAs) have boosted their power conversion efficiencies (PCEs) exceeding 18% [1, 6–19]. Aside from SMA-based ones, the pioneer work on firstly polymerized small-molecular acceptors (PSMAs) via polymerization of a large π-fused SMA building block (IDIC16) with a thiophene unit, namely PZ1, was reported by Zhang et al. in 2017, where PZ1 exhibits a low bandgap and high absorption coefficient, resulting in a relatively high PCE in the PSCs [3, 20]. After that, all polymer solar cells (all-PSCs) comprising P_D and PSMAs in the active layers have quickly achieved PCEs of over 16%, which show the unique merits of superior morphological stabilities of devices under thermal or mechanical stress and good compatibility with large-scale manufactures such as roll-to-roll printing [2–5, 20–33]. Nevertheless, the presence of rigid backbones in such fully conjugated polymers significantly decreases their solubility, and induces strong aggregation of polymers in the solid states, often leading to unoptimized morphology and unsatisfactory mechanical properties of the resulting active layers. It has been demonstrated that the introduction of flexible conjugation-break spacers (FCBSs) (*i.e.*, aliphatic segments) into a rigid P_D or polymer acceptor (P_A) skeleton is an effective strategy for alleviating their backbone rigidity and thus significantly enhancing the solubility of generating polymers and mechanical properties of the resulting PSCs [34–39].

Recently, our group has pioneered two non-fully conjugated PSMAs, PF1-TS4 and PFY-2TS, by copolymerizing fixed lengths of FCBSs with advanced SMAs, IDIC16 and Y6 derivatives to obtain PCEs of 8.6% and 12.3%, respectively, with enhanced thermal stabilities in their all-PSCs [38–40]. In addition, the introduction of FCBSs into polymer backbones for realizing the equilibrium between PCE and mechanical properties has been reported. For example, Kim et al. reported a high PCE of 17% and a crack onset strain (COS) of 12% in the PSCs based on the P_D containing the FCBS unit [35]. Furthermore, our group reported a series of P_As by including different contents of FCBS, demonstrating that an all-PSC based on PYTS-0.3 (incorporating 30% FCBS, as P_A) and PBDB-T (as P_D) realized high photovoltaic (PV) performance with its PCE of 14.7% and robust mechanical properties with COS of 21.6% [34]. These results revealed that the incorporation of appropriate FCBSs in copolymers (either P_Ds or P_As) could significantly enhance solution processability, thermal stability, and mechanical ductility of PSCs, while maintaining their satisfied PV performance. However, the selection of FCBS lengths in those systems has been in a mode of "trial-and-error", without exploring any systematic studies on impacts of FCBS lengths in P_As on their PV- and mechanical-properties of PSCs, although some polymers with different lengths of FCBSs have been employed in the field of organic field-effect transistors (OFETs) [37, 41–45].

In this work, we develop a series of non-conjugated P_As, PYT(S)-Cn, polymerized from a conjugated Y5 derivative (YBO-Br) and bis(trimethylstannyl)-bithiophene with different thio-aliphatic lengths as FCBSs between two thiophene units (TS-Cn, n stands for 0 (as a control-polymer without C-S bonds either), 2, 4, and 8 carbon atoms), through simple synthetic routes (Scheme S1). The introduction of S atom is mainly for the ease of the synthesis of FCBSs and moreover, sulfur has a balanced weak electron donating nature and moderate π-electron accepting capability into its 3d-orbitals when connected to aryl groups, which may be able to tune the highest occupied molecular orbital (HOMO) levels of the resulting polymers [46]. The incorporation of FCBSs with different lengths is found to considerably affect the solubility and molecular flexibility of the resulting P_As. Interestingly, with the increase of FCBS lengths, P_As show enhanced inter/intramolecular packings with higher crystallinity, decreased solubility and miscibility with P_D. As a result, all-PSCs based on PYTS-C2 incorporated the shortest length of FCBS (2 carbon atoms) achieve a high PCE_{avg} of 11.20% (PCE_{max} of 11.37%), which significantly outperforms those of PYTS-C4 (PCE_{avg} = 3.37%) and PYTS-C8 (PCE_{avg} = 2.74%) containing longer FCBS, as well as that of rigid fully conjugated PYT-C0 without FCBS (PCE_{avg} = 4.84%). We found that this significant difference in the PV performance is mainly due to enhanced exciton dissociation, suppressed monomolecular/trap-assisted recombination, optimized morphology, and high domain purity. Importantly, among the blends involving PBDB-T:PYT(S)-Cns, the blend with PYTS-C2 shows the best mechanical properties with a

https://doi.org/10.1007/s40820-022-00884-8

COS of 12.39% and a toughness of 2.09 MJ m^{-3}, being at least two times higher than those of other blends with P_As of PYTS-C4, PYTS-C8, and PYT-C0 (COS = 6.03%, 4.77%, and 2.75%, and toughness = 0.68, 0.45, and 0.06 MJ m^{-3}, respectively). This study demonstrates the success of integrating FCBS with the appropriate length into polymer conjugated backbone in improving solubility, mechanical ductility, and high efficiency of its corresponding all-PSCs.

2 Experimental Section

2.1 Materials

YBO-Br was synthesized according to the reference [47]. Thiophene, sulfur powder, 1,2-dibromoethane, 1,4-dibromobutane, 1,8-dibromooctane, *n*-butyl lithium, $Pd_2(dba)_3$, and P(*o*-Tol)$_3$ were purchased from Sigma-Aldrich. 5,5'-bis(trimethylstannyl)-2,2'-bithiophene (T-C0-Sn) was purchased from Suzhou GR-chem Pharma Tech Co., Ltd. Poly[(2,6-(4,8-bis(5-(2-ethylhexyl)thiophen-2-yl)-benzo[1,2-*b*:4,5-*b*']dithiophene))-*alt*-(5,5-(1,3′-di-2-thienyl-5,7′-bis(2-ethylhexyl)benzo[1,2′-*c*:4′,5′-*c*′]dithiophene-4,8-dione))] (PBDB-T) was purchased from Brilliant Matters.

2.2 Device Fabrication

The normal type all-PSCs (indium tin oxide (ITO)/poly(3,4-ethylenedioxy thiophene):polystyrene sulfonic acid (PEDOT:PSS, AI4083 from Heraeus)/active layer/interlayer/Ag) were fabricated by following processes. Poly[[2,7-bis(2-ethylhexyl)-1,2,3,6,7,8-hexahydro-1,3,6,8-tetraoxobenzo[lmn][3,8]phenanthroline-4,9-diyl]-2,5-thiophenediyl[9,9-bis[3'((N,N-dimethyl)-N-ethylammonium)]-propyl]-9H-fluorene-2,7-diyl]-2,5-thiophenediyl] (PNDIT-F3N-Br) was used as interfacial layer. ITO-coated glass substrates were washed by ultrasonication with deionized-water, acetone and isopropyl alcohol in series. The cleaned substrates were, dried for more than 1 h at 80 °C. A plasma treatment was proceeded for 10 min before spin-casting PEDOT:PSS solution. The PEDOT:PSS solution was spin-casted at 3000 rpm for 30 s, then thermally annealed at 165 °C for 15 min in ambient condition. Then, the samples were carried to a N_2-filled glovebox. Next, the P_D-P_A blend solutions with optimal concentration (12 mg mL^{-1}) and P_D:P_A ratio (1:1.2) were prepared in chloroform (CF). The solutions were stirred for at least 1 h at 55 °C before spin-coating. Then, the solutions were spin-casted onto the PEDOT:PSS-coated ITO substrates at 1750 rpm for 30 s, and the films were thermally annealed at 100 °C for 5 min. Then, the samples were stored in a high-vacuum chamber for 2 h to remove residual solvents in the films. Then, the PNDIT-F3N-Br solution (1 mg mL^{-1} in methanol) was spin-coated onto the active layer films with 3000 rpm for 30 s. Finally, Ag electrode (120 nm) was deposited by thermal evaporation in an evaporation chamber, under a high vacuum (~ 10^{-6} Torr) condition. The photoactive area of the all-PSC devices is 0.042 cm^2, measured from the optical microscopy.

2.3 Pseudo Free-standing Tensile Test

The films for the pseudo free-standing tensile test were prepared under the same condition with all-PSC fabrication. The films were spin-casted onto the PSS-coated glass substrate and cut into a dog-bone shape by a femtosecond laser. Then the films were floated onto the water surface, and attached to the grips by Van-der Walls interaction. The strain was applied with a fixed strain rate (0.8×10^{-3} s^{-1}), and the tensile load values were measured by a load cell with high resolution (LTS-10GA, KYOWA, Japan). Elastic modulus was calculated using least square method for the slope of the linear region in stress-strain curve.

3 Results and Discussion

3.1 Synthesis and Characterization of PYT(S)-Cns

The chemical structures of P_D and P_As used in this study are illustrated in Fig. 1a. PBDB-T was employed as P_D due to its matched energy levels and complementary optical absorption with those of a series of P_As [48]. We chose PYT-C0 as the reference P_A due to its fully conjugated rigid structure. Segments of thioalkyl with thiophene ends (TS-Cn) containing different lengths (highlighted in red in Fig. 1a) were incorporated into the backbone of PYT-C0 to provide different degrees of backbone flexibility between the conjugated YBO cores. The P_As were synthesized via

Stille coupling polymerization of YBO-Br with T-C0-Sn or TS-Cn-Sn as FCBS units (Scheme S1). The resulting copolymer acceptors were named PYT-C0 and PYTS-Cn, where n = 2, 4, and 8, respectively, denoting the number of carbon atoms between the thiophene units in FCBSs. The number-average molecular weights (M_ns) of PYTS-Cn polymers are in the range of 23 to 40 kg mol^{-1} as evaluated by gel permeation chromatography (GPC) (Table 1). In case of PYT-C0, the solubility was poorer compared to the FCBS-incorporated P_As, thus limiting its M_n growth during the polymerization. The decomposition temperatures (T_d, 5% mass loss) of the P_As were found as high as 331–349 °C in thermogravimetric analysis (TGA) (Fig. S1), which indicates that all P_As have good thermal stability without negative effect by the incorporation of FCBS. The solubilities of the polymers were measured and summarized in Fig. S2 and Table S1. The electrochemical properties of the polymers were investigated via cyclic voltammetry (CV) measurements and outlined in Figs. 1b and S3, Table S2. The diagram of energy levels of P_As and P_D are illustrated in Fig. 1b, indicating that all P_As possess well-aligned HOMO and lowest unoccupied molecular orbital (LUMO) energy levels in connection with P_D for effective all-PSC operation. It was noted that PYT-C0 shows slightly higher HOMO and lower LUMO levels compared to PYTS-Cn with FCBSs, which is probably due to its slightly longer conjugated length without FCBS as indicated in density functional theory (DFT) simulation (see below) [45].

The absorption spectra of the polymers were measured in both CF solutions and the solid states as shown in Fig. S4. The PBDB-T presents complementary absorption spectrum to those of the P_As. PYT-C0 exhibits noticeably blue-shifted absorption spectrum as compared to the other P_As with FCBS probably due to different molecular conformations and aggregation states in solutions. All P_As with FCBS showed similar λ_{max} and optical bandgap in films, which may be due to their comparably effective conjugation lengths and compact packing for all P_As in solid states (Fig. S4). However, for PYT-C0 film, its λ_{max} presents a considerable bathochromic shift of ca. 30 nm compared with other PYTS-Cn polymers, led by large aggregates originated from its rigid backbone when processed into films. Therefore, we assumed that the incorporation of bis(thioalkyl thiophene) could donate backbone flexibility and solution processability on P_As. To further investigate the effects of FCBS lengths on the aggregation properties of the P_As, temperature-dependent ultraviolet-visible absorption spectra of the P_As in CF solution were measured (Fig. S5) [34, 35, 49–51]. First, all P_As exhibited blue-shifted maximum absorption peaks and gradually decreased absorption intensity as temperature increased, which indicates that the P_As tended to aggregate at room temperature, and gradually disaggregated at higher temperatures [41, 52, 53]. In addition, such absolute blue-shifts for P_As from 20 to 60 °C were gradually enhanced with increasing of FCBS lengths in the order of 8 nm for PYTS-C2, 16 nm for PYTS-C4, and 27 nm for PYTS-C8. Correspondingly, a gradual blue-shift of maximum absorption peak for PYTS-Cns in CF solution at 60 ℃ was observed with increasing of FCBS length (Fig. 1c). This indicates that longer FCBSs enable molecular conformations and backbone-twisting of P_As to be more temperature-dependent. In addition, PYT-C0 in CF solution showed a less pronounced blue-shift of 10 nm from 20 to 60 °C, which could be due to its stronger intermolecular aggregation caused by rigid and planar conjugated skeleton. This factor makes it difficult to disaggregate at high temperature (Fig. S5). This is also supported by the fact that PYTS-C2, PYTS-C4, and PYTS-C8 exhibit much better solubilities in CF when the temperature increases from 20 to 50 °C, while the solubility of PYT-C0 remains poor even at 50 °C. As anticipated, the fully conjugated polymer PYT-C0 exhibited inferior solubility of 0.7 mg mL^{-1} in CF solution (at 50 °C) among P_As, which may be resulted from strong interchain aggregation of rigid backbone. For PYTS-Cns, the solubilities clearly increased when FCBSs incorporated in the polymer backbones, and they are varied depending on the lengths of FCBSs, measured as 39.8, 39.1, and 16.8 mg mL^{-1} for the PYTS-C2, PYTS-C4, and PYTS-C8 (Table S1), respectively. To investigate the effects of FCBS lengths on the solubilities of the P_As, grazing-incidence wide-angle X-ray scattering (GIWAXS) measurements were performed. PYTS-C8 showed larger crystal coherence lengths of $L_{c,100}^{IP}$ of 6.05 nm in the in-plane (IP) direction and $L_{c,010}^{OOP}$ of 2.14 nm in the out-of-plane (OOP) direction compared to those of PYTS-C2 ($L_{c,100}^{IP}$ = 0.88 nm, $L_{c,010}^{OOP}$ = 1.90 nm) and PYTS-C4 ($L_{c,100}^{IP}$ = 0.99 nm, $L_{c,010}^{OOP}$ = 1.80 nm). Moreover, PYT-C0 showed relatively large $L_{c,100}^{IP}$ of 5.04 nm and $L_{c,010}^{OOP}$ of 2.32 nm, which are shown in Fig. S6 and Table S3. These values indicate that the excessive aggregation and crystalline properties were effectively alleviated by the introduction of FCBS into PYT-C0, resulting in better solubilities for the PYTS-C2 and

 https://doi.org/10.1007/s40820-022-00884-8

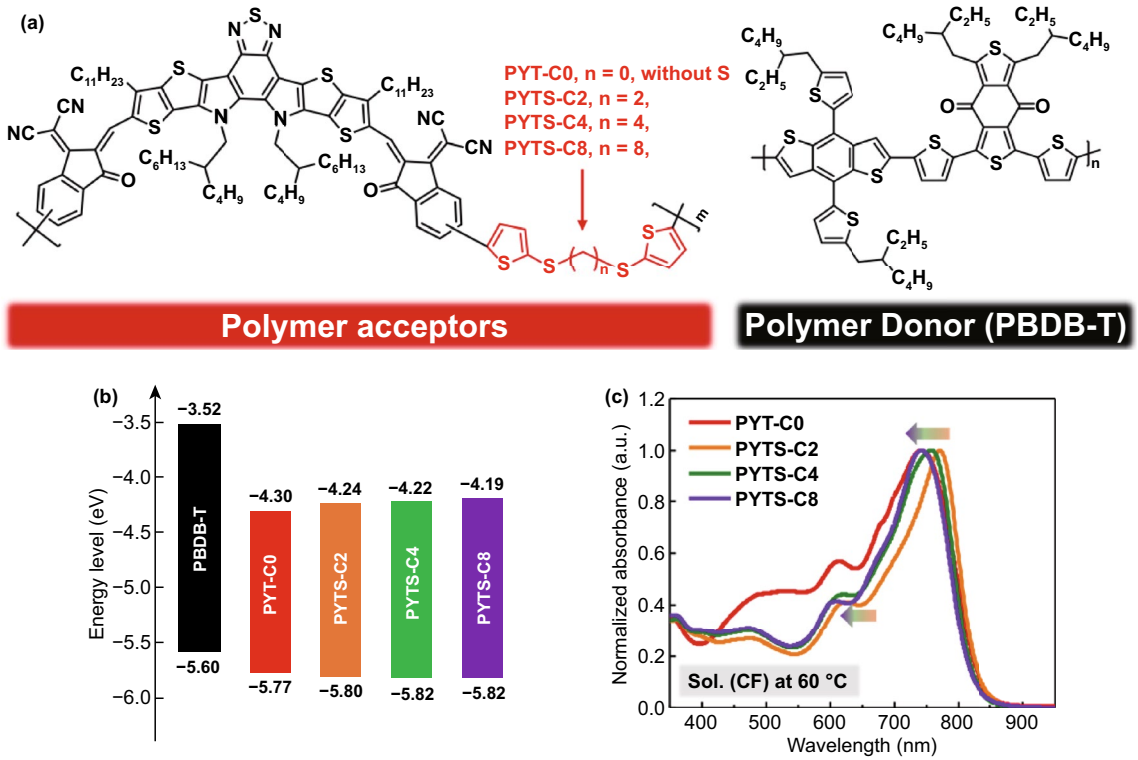

Fig. 1 **a** Chemical structures of PYT(S)-Cn as the P_As and PBDB-T as the P_D. **b** Molecular energy levels of PBDB-T and PYT(S)-Cns obtained from cyclic voltammetry measurements. **c** Normalized absorption spectra of the P_As in CF solution at 60 °C

Table 1 Molecular weight-, optical-, and electrochemical-properties of the active materials used in this study

Polymer	M_n [kg mol^{-1}]	*PĐI*	$\lambda_{max}^{sol,\ 20\ °C}$ [nm][a]	$\lambda_{max}^{sol,\ 60\ °C}$ [nm]	λ_{max}^{film} [nm][a]	λ_{onset}^{film} [nm][a]	E_g^{opt} [eV][b]
PBDB-T	43.0	2.78	610	-	572	673	1.84
PYT-C0	16.8	2.43	752	742	818	957	1.30
PYTS-C2	39.9	1.77	779	771	788	866	1.43
PYTS-C4	29.9	3.04	774	758	785	865	1.43
PYTS-C8	23.2	4.28	772	745	789	866	1.43

[a] Obtained from Fig. S4; [b] calculated as $1240/\lambda_{onset}^{film}$

PYTS-C4 polymers. However, the presence of FCBSs longer than a certain length increased the aggregation and crystallinity again, leading to reduced solubility and increased crystal sizes, as proven in the case of PYTS-C8.

DFT calculations were performed to reveal the optimized molecular structures, frontier molecular orbitals, and origins of optical spectra differences for P_As with different lengths of FCBSs. The chemical model of two YBO cores linked one bithiophene or FCBS with methyl side chains instead of the bulky ones was chosen for simplifying the calculations. As illustrated in Figs. S7 and S8, respectively, PYT-C0 showed a relatively planar Z-shape configuration with a rigid backbone due to the centrosymmetric bithiophene linkage. This may be the reason for its strong intermolecular π-π aggregation and therefore relatively high crystallinity, resulted in its poor solubility (Tables S1 and S3). However, all PYTS-Cn with FCBS showed C-shape configurations and two YBO cores are found in different planes after structural optimizations, which might be the reasons for their entirely different aggregation behaviors from PYT-C0. Furthermore, the

HOMO and LUMO of all PYTS-Cns exhibited similar charge distribution on only YBO cores instead of the FCBS linkage, which indicated that all PYTS-Cn have comparably effective conjugation lengths. As a comparison, HOMO of PYT-C0 is distributed along the whole YBO core and bithiophene linkage structure, which greatly promotes charge transfers (Fig. S8). It is expected that these different HOMO and LUMO distribution could induce the differences of absorption spectra between PYT-C0 and PYTS-Cns, as shown in theoretical calculation of their electronic excitations and absorption spectra (Figs. S4, S9 and S10, Table S4).

3.2 Photovoltaic Properties

Next, we investigated the PV properties of all-PSC devices with a normal geometry of ITO/PEDOT:PSS/active layer/PNDIT-F3N-Br/Ag. The detailed device structures and fabrication procedures are described in Supporting Information. The current density–voltage (*J*–*V*) curves under optimized condition and corresponding PV parameters are presented in Fig. 2a and Table 2. The PBDB-T:PYT-C0-based all-PSCs show a low PCE_{avg} of 4.84% with an open-circuit voltage ($V_{oc,\ avg}$) of 0.92 V, and an average short-circuit current density ($J_{sc,\ avg}$) of 11.99 mA cm^{-2}. Notably, the all-PSCs based on the PBDB-T:PYTS-C2 blend exhibit a high PCE_{avg} of 11.20% (PCE_{max} = 11.37%) with its $J_{sc,\ avg}$ of 18.45 mA cm^{-2}, and a fill factor (FF_{avg}) of 0.66. In contrast, the PCE_{avg}s of PYTS-C4- and PYTS-C8-based all-PSCs with longer FCBS units decreased to 3.37% and 2.74%, respectively. These significant differences in PCEs indicate that the FCBS lengths in P_As have a significant impact on PV performance of all-PSCs. The external quantum efficiency (EQE) spectra are shown in Fig. 2b. The calculated J_{sc} values from the EQE spectra agreed well with the ones obtained from the *J*-*V* curves within 4% deviations (Table 2). Compared with those of other blends of PYT-C0, PYTS-C4, and PYTS-C8, PBDB-T:PYTS-C2 blends showed higher EQE responses over the full absorption range (300–900 nm). These results suggest that the active layer based on PYTS-C2 is optimal to obtain more efficient charge generations from both P_D and P_A absorption ranges than the others. Additionally, it was found that all-PSCs based on PYTS-C2 with higher molecular weight exhibits better PCE of 11.37% compared to that of PYTS-C2 with lower molecular weight (PCE = 9.11%) (Fig. S11 and Table S5), which may indicate that the high molecular weight polymer helps to promote morphology optimization and device performance improvement [53, 54].

In order to further clarify the reasons for the different PV performances of all-PSCs, we examined the charge generation, transport, and recombination mechanisms of the PBDB-T:P_A blends. First, the charge generation properties of blends were explored by calculating the exciton dissociation probabilities (*P*(E,T)) from the curves of photocurrent density (J_{ph}) versus effective voltage (V_{eff}) over the saturated photocurrent density (J_{sat}, at V_{eff} = 2.5 V) (Fig. 2c). The *P*(E,T) values significantly increased from 72.6% for PBDB-T:PYT-C0 to 94.2% for PBDB-T:PYTS-C2 blend, and, then, decreased to 78.6% for PBDB-T:PYTS-C4 and 75.4% for PBDB-T:PYTS-C8. This suggests that the PBDB-T:PYTS-C2 blend has superior charge generation abilities at the donor:acceptor (D:A) interfaces to the other blend systems. Subsequently, the space charge limited current (SCLC) mobilities for the blend films were measured to investigate their charge transport properties (Table S6). Both hole mobility (μ_h) and electron mobility (μ_e) values of the PBDB-T:PYTS-C2 blend were higher than those of the other blends (*i.e.*, 1-order lower μ_e in magnitude), supporting its higher J_{sc} value.

The dependences of V_{oc} and J_{sc} on light intensity (*P*) were also measured to examine the charge recombination properties of the blends (Figs. 2d and S12). Generally, V_{oc} of all-PSC is proportional to the natural logarithm of *P* ($V_{oc} = S \times \ln(P)$), with the unit of $kT\ q^{-1}$ (where k = Boltzmann constant, T = temperature and q = elementary charge), and its slope (*S*) approaches unity when no monomolecular or trap-assisted recombination occurs before charge collection on electrodes [55]. Notably, the *S* values for PYT-C0 and PYTS-C2 are similar (1.25 and 1.27 respectively), and gradually increase with the increasing lengths of FCBSs (1.46 for PYTS-C4, and 1.61 for PYTS-C8) (Fig. 2d). This indicates that incorporating short FCBS units in the P_As, particularly TS-C2, do not influence monomolecular or trap-assisted recombination of the all-PSCs, but incorporation of the longer FCBS units (TS-C4 and TS-C8) negatively affect the monomolecular or trap-assisted recombination properties. Additionally, J_{sc} and *P* follow the relationship of $J_{sc} \propto P^{\alpha}$, where α as the power-law component would be close to 1 when the bimolecular recombination in devices is negligible [56]. The PBDB-T:PYT-C0 blend showed a lower α value of 0.88 than those of the other blends PYTS-Cns

https://doi.org/10.1007/s40820-022-00884-8

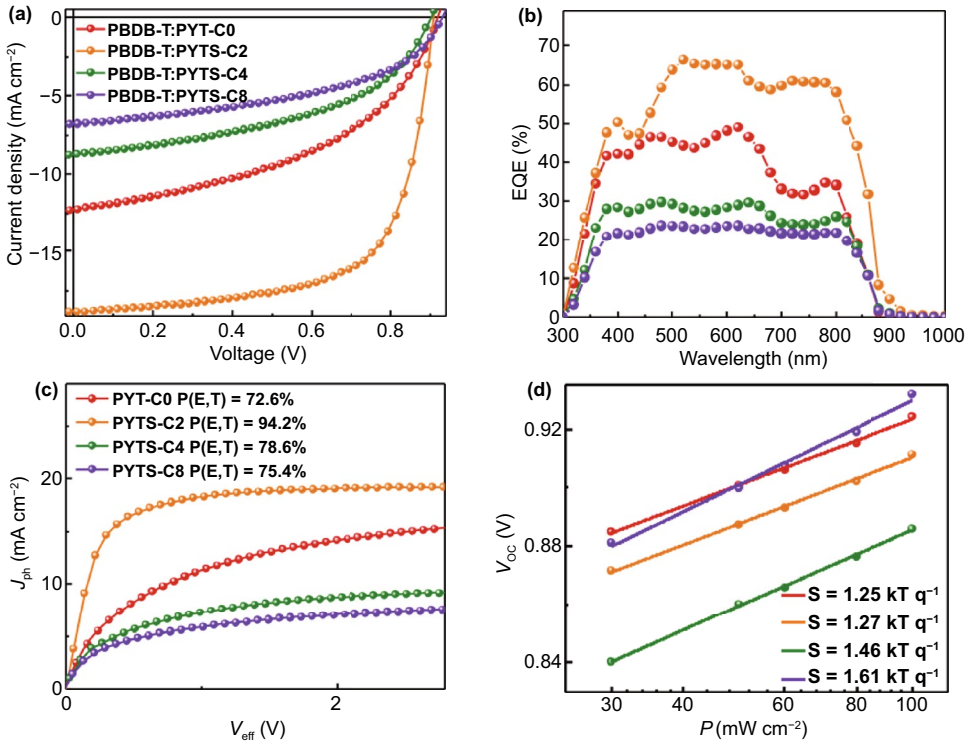

Fig. 2 **a** *J*–*V* curves; **b** EQE response spectra; **c** J_{ph} vs. V_{eff} curves; **d** Dependences of V_{oc} on light intensities for the all-PSCs

Table 2 PV performances of the all-PSCs depending on the lengths of FCBSs in P_As

P_A	V_{oc} [V][a]	J_{sc} [mA cm^{-2}][a]	Calc. J_{sc} [mA cm^{-2}]	FF[a]	$PCE_{avg\ (max)}$ [%][a]
PYT-C0	0.92 ± 0.01	11.99 ± 0.7	12.19	0.44 ± 0.02	4.84 ± 0.31 (5.15)
PYTS-C2	0.91 ± 0.01	18.72 ± 0.43	18.45	0.66 ± 0.02	11.20 ± 0.14 (11.37)
PYTS-C4	0.90 ± 0.01	8.01 ± 0.52	8.28	0.47 ± 0.01	3.37 ± 0.28 (3.73)
PYTS-C8	0.92 ± 0.01	6.33 ± 0.32	6.87	0.47 ± 0.00	2.74 ± 0.16 (2.97)

[a] All parameters represent average values measured from five to ten all-PSC devices

($\alpha = 0.92$–0.94). This indicates that the bimolecular recombination properties of the all-PSCs are improved through the incorporation of FCBSs in the P_As (Fig. S12). The above mentioned results from the charge generation and recombination properties support the increased J_{sc} and FF values in the PBDB-T:PYTS-C2 blends compared to the other PBDB-T:P_As blends.

3.3 Thin-film Mechanical Properties

The mechanical properties of the blend films were studied using a pseudo free-standing tensile test method [57, 58]. Thin-film samples of P_D:P_As blends for mechanical testing were prepared under the same conditions as those of all-PSC blend films, and the tensile test results are shown in Fig. 3a-b and Table 3. Interestingly, PBDB-T:PYTS-C2 blend films showed superior COS of 12.39% with toughness of 2.09 MJ m^{-3}, which are four times for the former and thirty times for the latter higher than those of PYT-C0 based blend films (COS = 2.75% and toughness = 0.06 MJ m^{-3}). In addition, the COS and toughness values decreased rapidly with increased lengths of FCBSs (COS of 6.03% and 4.77%, toughness of 0.68 and 0.45 MJ m^{-3} for PBDB-T:PYTS-C4, and PBDB-T:PYTS-C8 blends, respectively). To further understand the difference in the mechanical properties of the blend films, the pristine films of polymer acceptors

were also tested. However, except PYTS-C2, all other polymer acceptor films are very brittle, and no mechanical data can be obtained, which may relate to their relatively poor film-forming ability and strong crystallinity. The COS and toughness value for PYTS-C2 were 2.81% and 0.34 MJ m^{-3}, respectively (Fig. S13 and Table S7). This indicates that the short FCBS length from TS-C2 incorporated into the conjugated polymer backbone could be optimal to afford simultaneously improved PV performance and mechanical properties.

From the optical microscopy (OM) images of the tensile bars before testing, it can be seen clearly different initial morphologies of the blends depending on the P_As (Fig. 3c, upper images). The PBDB-T:PYT-C0 blend showed locally formed and large-sized defects in its film (grey dots), whereas the PBDB-T:PYTS-C2 blend exhibited more uniform and smoother surfaces with very few defects or agglomerates in the non-strain image. In comparison, the PBDB-T:PYTS-C4 and PBDB-T:PYTS-C8 blends displayed defects and agglomerates throughout the films, but with a smaller size than those of the PBDB-T:PYT-C0 blend. These different initial morphologies have influences to their crack propagation processes in the images of the strained films (Fig. 3c, lower images). The PBDB-T:PYT-C0, PBDB-T:PYTS-C4, and PBDB-T:PYTS-C8 blends showed many cracks being propagated around defect sites. These original cracks and defects in films accelerated the mechanical failures under further strains due to stress concentrations [33]. In contrast, the PBDB-T:PYTS-C2 blend exposed no such crack propagations, indicating that the uniform film is able to efficiently dissipate the mechanical stresses under the strains. The combined results of mechanical tests and OM images demonstrate that the incorporation of FCBS of appropriate length (*i.e.* two carbon atoms in this work) in the polymer acceptors not only provides the flexibility to polymer chains, but also allows the formation of optimal blend morphology without excessive aggregation and phase separation, bringing high mechanical strength and stretchability for the active layers.

3.4 Morphological Properties

To further explore the origins of the different PV- and mechanical-properties of the PBDB-T:P_A blends, morphology studies were examined with combined measurements of resonant soft X-ray scattering (RSoXS), atomic force microscopy (AFM), GIWAXS, and OM, as shown in Fig. 4, Table 4 and Fig. S14. First, the RSoXS profiles were obtained under a beam energy of 284.4 eV, which can maximize the material contrast between P_D and P_As [59, 60]. Relative domain purity, which is proportional to square root of integrated scattering intensity, was calculated for more quantitative analysis [59, 61]. All blends showed distinguishable peaks and significantly different domain-spacings and -purities (Fig. 4a and Table 4). As a result of increasing FCBS lengths in P_As, *d*-spacing values gradually increased, while the domain purities decreased. The PBDB-T:PYTS-C2 blend exhibited a small domain spacing (*d*-spacing = 61 nm) and a high relative domain purity of 1.00, compared with those of PBDB-T:PYTS-C4 blend (*d*-spacing = 242 nm, relative domain purity = 0.79) and PBDB-T:PYTS-C8 blend (*d*-spacing = 349 nm, relative domain purity = 0.82). It suggests that the presence of TS-C2 FCBS in P_A is effective to afford a smaller domain size and higher domain purity, thereby promoting efficient charge separation and charge transportation of all-PSCs [53, 54]. A similar trend of the surface roughness of PBDB-T:P_As blends depending on the lengths of FCBSs was observed in the AFM 3D height images (Fig. 4b and Table 4). The root-mean-square average roughness (R_q) for PBDB-T:PYTS-C2, PBDB-T:PYTS-C4, and PBDB-T:PYTS-C8 blends were 1.6, 4.3, and 16.0 nm, respectively. This indicates that the further increase of FCBS lengths induces large phase segregation between P_D and P_As, which is also consistent with not only the decreased solubility in the case of PYTS-C8, but also their decreased charge generation and transport, therefore lower J_{sc} and FF, and finally lower PCEs as discussed earlier. On the other hand, the PYT-C0 based blend film did not show a distinct peak in RSoXS and exhibited an extremely large R_q of 23.3 nm in the AFM height image. We speculate that the peak of the PYT-C0 based blend film could not be detected in the measured *q* range of RSoXS due to its too large domain size. Furthermore, the OM images also showed a very non-uniform film with large aggregates in the PBDB-T:PYT-C0 blend (Fig. 4c). In contrast to the very rough and non-uniform surface of PBDB-T:PYTS-C8 blend film, the PBDB-T:PYTS-C2 and PBDB-T:PYTS-C4 blend films displayed a relatively uniform surface. Therefore, the results from the AFM, RSoXS and OM measurements show the same trend for the PBDB-T:P_A blend films.

https://doi.org/10.1007/s40820-022-00884-8

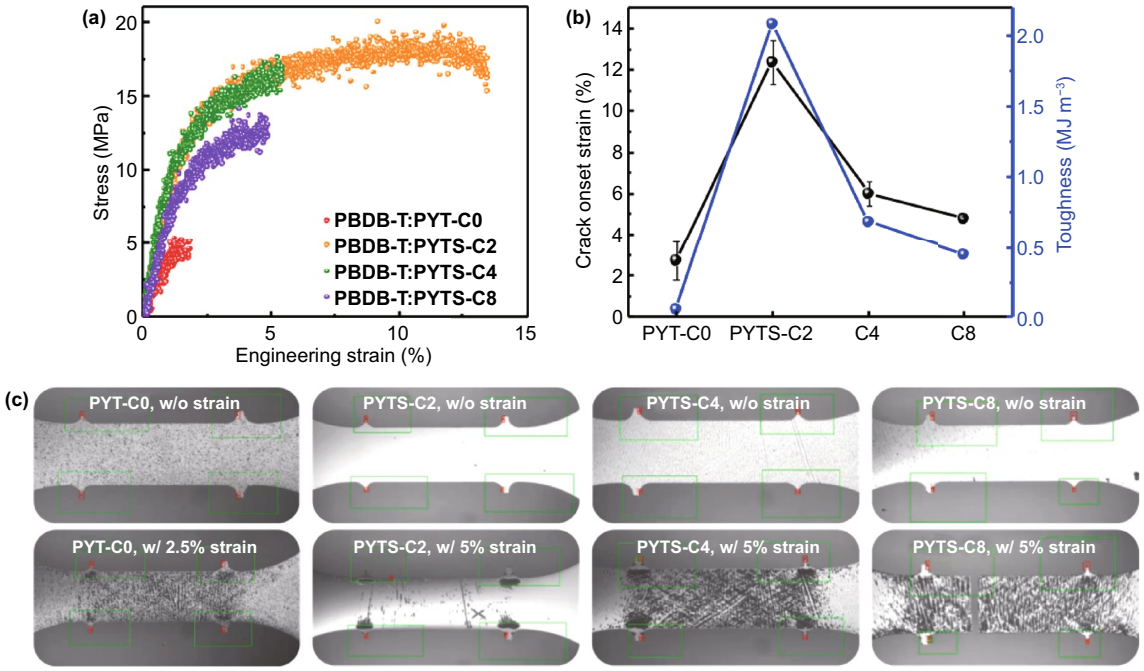

Fig. 3 **a** *Stress–Strain* curves for the PBDB-T:P_As blends, and **b** Plots of COS and toughness values of the blends depending on the P_As. **c** Tensile-specimen images of the four blends during measurement without strain (upper images) and with 2.5% (PYT-C0) and 5% engineering strain (lower images). The green and red boxes indicate regimes for displacement tracking by digital image correction camera

Table 3 Mechanical properties of the PBDB-T:P_As blends measured from the pseudo free-standing tensile test

Blend	E [Mpa][a]	COS [%][a]	Toughness [MJ m^{-3}][a]
PBDB-T:PYT-C0	514	2.75	0.06
PBDB-T:PYTS-C2	649	12.39	2.09
PBDB-T:PYTS-C4	914	6.03	0.68
PBDB-T:PYTS-C8	626	4.77	0.45

[a] All parameters represent average values from 3 samples

Another investigation of different blends morphology depending on the P_As was performed by comparing the crystalline properties of PBDB-T:P_As blends using the GIWAXS measurements (Fig. S14 and Table S8). It is found that the L_c values of the (100) peaks in the IP direction increased from 10.39 nm for PBDB-T:PYTS-C2 to 11.09 nm for PBDB-T:PYTS-C4 and 13.04 nm for PBDB-T:PYTS-C8. In comparison, the PBDB-T:PYT-C0 blend shows a relatively high IP L_c value of 11.32 nm. The L_c values for the (010) peaks in the OOP direction for all PBDB-T:P_A blends showed a similar trend with IP (100) peaks (Table S8). These results indicate that incorporation of short TS-C2 FCBS could effectively decrease the crystallinity of the fully conjugated P_A in the blends. However, longer FCBSs than TS-C2 in P_As resulted in rather increased crystallinity in the blends. Additionally, the interfacial tensions between P_As and P_D were calculated by measuring the pristine film contact angle of materials using glycerol and water droplets by means of Wu method (Table S9). PYTS-C2 and PYTS-C4 films showed lower interfacial tension values of 1.38 and 1.44 mN m^{-1} when paired with PBDB-T than those of the PYT-C0-based (6.31 mN m^{-1}) and PYTS-C8-based blends (2.82 mN m^{-1}). This supports that PYTS-C2 and PYTS-C4 have better compatibility with PBDB-T compared to the remaining ones [62]. These lower interfacial tensions of PYTS-C2 and PYTS-C4 could reduce the degree of their phase-separations and decrease the domain size in the blend [63].

Based on the evaluated results of the above morphology analyses, PBDB-T:PYT-C0 blend shows large aggregates and segregated domains compared with those of PBDB-T:PYTS-Cn blends. These are mainly due to the low solubility of PYT-C0 polymers inducing the excessively large aggregates and poor mixing with P_D. In this case, the excessively segregated blend morphology decreases charge dissociation, increases

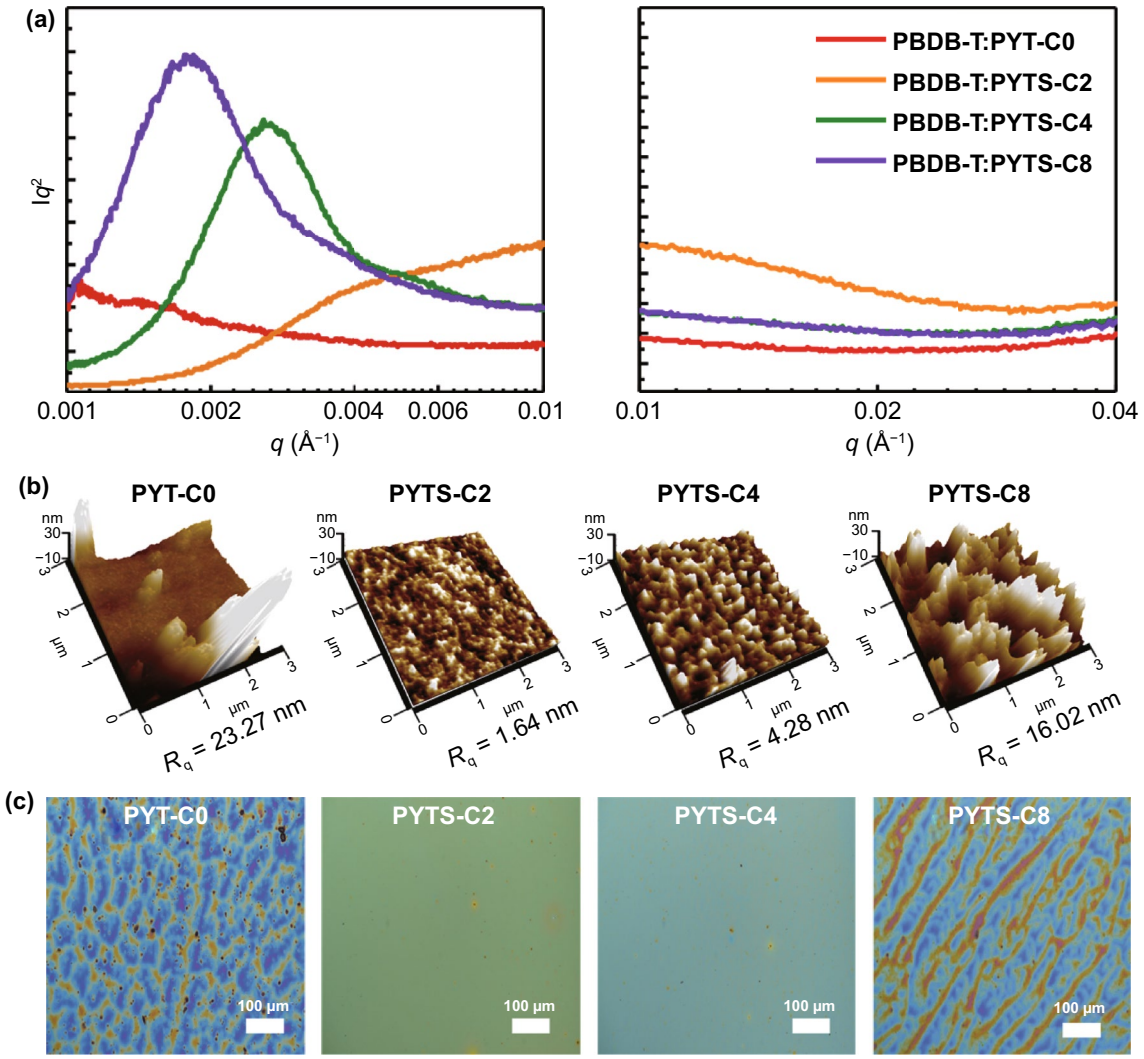

Fig. 4 **a** RSoXS profiles, **b** AFM 3D height images, and **c** OM images of the PBDB-T:P_As blend films

Table 4 Morphological characteristics of the PBDB-T:P_As blends

Blend [w/ PBDB-T]	*d*-spacing [nm][a]	Relative domain purity[a]	R_q^{AFM} [nm][b]
PYT-C0	–	–	23.3
PYTS-C2	61	1	1.6
PYTS-C4	242	0.79	4.3
PYTS-C8	349	0.82	16.0

[a] Estimated from the RSoXS profiles; [b] Obtained from AFM height images

bimolecular recombination and results in very poor mechanical stretchability in the blend (the left illustration of Fig. 5). On the other hand, when too long FCBS (over C4) is incorporated into the P_As, the blend film also exhibits severe phase-separation between P_D and P_A due to their less compatibility with P_D, even though the P_As showed reduced aggregate properties. These separated domains with low compatibilities can hinder the charge transfer to other domains, limiting the PV performances of all-PSCs. In addition, the sharp and weak interfaces between the domains could provide crack

https://doi.org/10.1007/s40820-022-00884-8

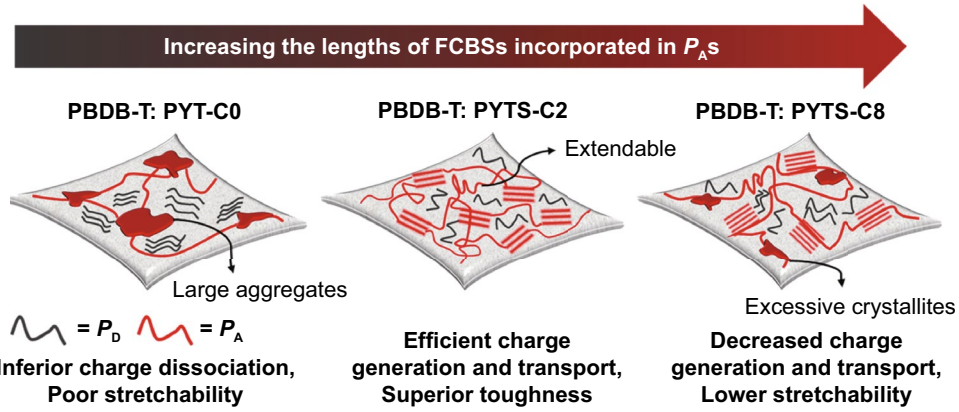

Fig. 5 Schematic illustration of the PBDB-T:PYT(S)-Cn blend morphologies with different length of FCBS

propagation pathways to degrade mechanical properties (the right illustration of Fig. 5).

Employing the optimal length of FCBS in P_A affords the excellent solubility in case of PYTS-C2 to prevent the formation of excessive aggregates and induce the superior compatibility with P_D. This morphology enables efficient charge separation and transport. The small domain sizes of the PBDB-T:PYTS-C2 film greatly reduce the crack propagation route and promote the extension of films without significant cracking during the stretching (the middle illustration of Fig. 5). Therefore, the PBDB-T:PYTS-C2 based all-PSCs showed not only high PCE of 11.37% but also superior mechanical properties (COS of 12.39%, toughness of 2.09 MJ m^{-3}). Overall, the length of FCBS integrated in P_A is an important factor in (i) controlling the P_A solubility; and (ii) increasing the compatibility between P_D and P_A, to achieve high PV performance and superior stretchability in all-PSCs.

4 Conclusions

In summary, we developed a new series of P_As by incorporating FCBS units with different lengths into the rigid backbone, thereby simultaneously enhancing the PV performance and mechanical robustness of all-PSCs. It was found that the incorporation of certainly short FCBS (PYTS-C2) endowed increased backbone flexibility, and thus prevented excessive aggregation, leading to the significantly increased solubility to the resulting P_As. However, the longer FCBSs (PYTS-C4 and PYTS-C8) increased intermolecular and/or intramolecular π-π stacking, causing decreased solubility and excessive aggregation, which resulted in poor compatibility with donor polymers and suboptimal morphology in forming films. As a result, the all-PSC based on PBDB-T:PYTS-C2 exhibited a PCE of 11.37%, which is superior to those of the devices based on PYT-C0 without FCBS and P_As with longer FCBSs. Moreover, the improved morphology of PBDB-T:PYTS-C2 blend realized higher mechanical stretchability and robustness with a COS of 12.39% and toughness of 2.09 MJ m^{-3}, compared with PBDB-T:PYT-C0 and PBDB-T:PYTS-Cn blends. Our findings demonstrate that introducing appropriate FCBS with short length, particularly TS-C2 for PYTS-C2, can simultaneously enhance the photovoltaic performance and mechanical robustness of the devices. Overall, this work inspires molecular design with rational FCBS selections for realizing highly efficient and mechanically robust all-PSCs that are appropriate for stretchable and flexible electronics.

Acknowledgements We thank the Swedish Research Council (2016-06146, 2019-02345), the Swedish Research Council Formas, the Swedish Energy Agency (52473-1), the Wallenberg Foundation (2017.0186 and 2016.0059) for financial support. This work was also supported by the National Research Foundation of Korea (NRF-2017M3A7B8065584 and 2020R1A4A1018516). Support from the National Natural Science Foundation of China (61774077), the Key Projects of Joint Fund of Basic and Applied Basic Research Fund of Guangdong Province (2019B1515120073), and the Research Fund of Guangdong-Hong Kong-Macao Joint Laboratory for Intelligent Micro-Nano Optoelectronic Technology (No. 2020B1212030010). Support from Sino-Danish Center for Education and Research is fully acknowledged. LRF, CFNM and CMA acknowledge Swedish Research Council (grant no. 2020-05223), Swedish Energy Agency (grant no. 45420-1), as well as the Swedish National Infrastructure for Computing (SNIC) at National Supercomputer Centre at Linköping University (NSC) for providing the computational infrastructure.

Funding Open access funding provided by Shanghai Jiao Tong University.

Supplementary Information The online version contains supplementary material available at https://doi.org/10.1007/s40820-022-00884-8.

References

1. W. Yang, Z. Luo, R. Sun, J. Guo, T. Wang et al., Simultaneous enhanced efficiency and thermal stability in organic solar cells from a polymer acceptor additive. Nat. Commun. **11**, 1218 (2020). https://doi.org/10.1038/s41467-020-14926-5
2. Q. Fan, W. Su, S. Chen, W. Kim, X. Chen et al., Mechanically robust all-polymer solar cells from narrow band gap acceptors with hetero-bridging atoms. Joule **4**(3), 658–672 (2020). https://doi.org/10.1016/j.joule.2020.01.014
3. Z.G. Zhang, Y. Li, Polymerized small-molecule acceptors for high-performance all-polymer solar cells. Angew. Chem. Int. Ed. **60**(9), 4422–4433 (2021). https://doi.org/10.1002/anie.202009666
4. T. Jia, J. Zhang, K. Zhang, H. Tang, S. Dong et al., All-polymer solar cells with efficiency approaching 16% enabled using a dithieno[3′,2′:3,4;2″,3″:5,6]benzo[1,2-c][1,2,5]thiadiazole (fDTBT)-based polymer donor. J. Mater. Chem. A **9**(14), 8975–8983 (2021). https://doi.org/10.1039/D1TA00838B
5. J. Zhang, C.H. Tan, K. Zhang, T. Jia, Y. Cui et al., π-extended conjugated polymer acceptor containing thienylene–vinylene–thienylene unit for high-performance thick-film all-polymer solar cells with superior long-term stability. Adv. Energy Mater. **11**(48), 2102559 (2021). https://doi.org/10.1002/aenm.202102559
6. Q. Liu, Y. Jiang, K. Jin, J. Qin, J. Xu et al., 18% efficiency organic solar cells. Sci. Bull. **65**(4), 272–275 (2020). https://doi.org/10.1016/j.scib.2020.01.001
7. Y. Lin, Y. Firdaus, F.H. Isikgor, M.I. Nugraha, E. Yengel et al., Self-assembled monolayer enables hole transport layer-free organic solar cells with 18% efficiency and improved operational stability. ACS Energy Lett. **5**(9), 2935–2944 (2020). https://doi.org/10.1021/acsenergylett.0c01421
8. W. Gao, H. Fu, Y. Li, F. Lin, R. Sun et al., Asymmetric acceptors enabling organic solar cells to achieve an over 17% efficiency: conformation effects on regulating molecular properties and suppressing nonradiative energy loss. Adv. Energy Mater. **11**(4), 2003177 (2021). https://doi.org/10.1002/aenm.202003177
9. S. Li, L. Zhan, Y. Jin, G. Zhou, T.K. Lau et al., Asymmetric electron acceptors for high-efficiency and low-energy-loss organic photovoltaics. Adv. Mater. **32**(24), 2001160 (2020). https://doi.org/10.1002/adma.202001160
10. S. Li, C.Z. Li, M. Shi, H. Chen, New phase for organic solar cell research: emergence of Y-series electron acceptors and their perspectives. ACS Energy Lett. **5**(5), 1554–1567 (2020). https://doi.org/10.1021/acsenergylett.0c00537
11. Y. Cui, H. Yao, J. Zhang, K. Xian, T. Zhang et al., Single-junction organic photovoltaic cells with approaching 18% efficiency. Adv. Mater. **32**(19), 1908205 (2020). https://doi.org/10.1002/adma.201908205
12. F. Qi, K. Jiang, F. Lin, Z. Wu, H. Zhang et al., Over 17% efficiency binary organic solar cells with photoresponses reaching 1000 nm enabled by selenophene-fused nonfullerene acceptors. ACS Energy Lett. **6**(1), 9–15 (2021). https://doi.org/10.1021/acsenergylett.0c02230
13. D. Li, C. Guo, X. Zhang, B. Du, C. Yu et al., Non-fullerene acceptor pre-aggregates enable high efficiency pseudo-bulk heterojunction organic solar cells. Sci. China Chem. **65**(2), 373–381 (2022). https://doi.org/10.1007/s11426-021-1128-1
14. L. Nian, Y. Kan, K. Gao, M. Zhang, N. Li et al., Approaching 16% efficiency in all-small-molecule organic solar cells based on ternary strategy with a highly crystalline acceptor. Joule **4**(10), 2223–2236 (2020). https://doi.org/10.1016/j.joule.2020.08.011
15. Z. Luo, R. Ma, T. Liu, J. Yu, Y. Xiao et al., Fine-tuning energy levels via asymmetric end groups enables polymer solar cells with efficiencies over 17%. Joule **4**(6), 1236–1247 (2020). https://doi.org/10.1016/j.joule.2020.03.023
16. W. Peng, Y. Lin, S.Y. Jeong, Z. Genene, A. Magomedov et al., Over 18% ternary polymer solar cells enabled by a terpolymer as the third component. Nano Energy **92**, 106681 (2022). https://doi.org/10.1016/j.nanoen.2021.106681
17. W. Guan, D. Yuan, J. Wu, X. Zhou, H. Zhao et al., Blade-coated organic solar cells from non-halogenated solvent offer 17% efficiency. J. Semicond. **42**(3), 030502 (2021). https://doi.org/10.1088/1674-4926/42/3/030502
18. C. Xu, Z. Zhao, K. Yang, L. Niu, X. Ma et al., Recent progress on all-small-molecule organic photovoltaics. J. Mater. Chem. A **10**, 6291–6329 (2022). https://doi.org/10.1039/D1TA10581G
19. C. Xu, X. Ma, Z. Zhao, M. Jiang, Z. Hu et al., Over 17.6% efficiency organic photovoltaic devices with two compatible polymer donors. Solar RRL **5**(8), 2100175 (2021). https://doi.org/10.1002/solr.202100175
20. Z.G. Zhang, Y. Yang, J. Yao, L. Xue, S. Chen et al., Constructing a strongly absorbing low-bandgap polymer acceptor for high-performance all-polymer solar cells. Angew. Chem. Int. Ed. **56**(43), 13503–13507 (2017). https://doi.org/10.1002/anie.201707678

21. H. Yu, S. Luo, R. Sun, I. Angunawela, Z. Qi et al., A difluoro-monobromo end group enables high-performance polymer acceptor and efficient all-polymer solar cells processable with green solvent under ambient condition. Adv. Funct. Mater. **31**(25), 2100791 (2021). https://doi.org/10.1002/adfm.202100791
22. H. Sun, B. Liu, Y. Ma, J.W. Lee, J. Yang et al., Regioregular narrow-bandgap n-type polymers with high electron mobility enabling highly efficient all-polymer solar cells. Adv. Mater. **33**(37), 2102635 (2021). https://doi.org/10.1002/adma.202102635
23. H. Fu, Y. Li, J. Yu, Z. Wu, Q. Fan et al., High efficiency (15.8%) all-polymer solar cells enabled by a regioregular narrow bandgap polymer acceptor. J. Am. Chem. Soc. **143**(7), 2665–2670 (2021). https://doi.org/10.1021/jacs.0c12527
24. Q. Fan, H. Fu, Q. Wu, Z. Wu, F. Lin et al., Multi-selenophene-containing narrow bandgap polymer acceptors for all-polymer solar cells with over 15% efficiency and high reproducibility. Angew. Chem. Int. Ed. **60**(29), 15935–15943 (2021). https://doi.org/10.1002/anie.202101577
25. Z. Luo, T. Liu, R. Ma, Y. Xiao, L. Zhan et al., Precisely controlling the position of bromine on the end group enables well-regular polymer acceptors for all-polymer solar cells with efficiencies over 15%. Adv. Mater. **32**(48), 2005942 (2020). https://doi.org/10.1002/adma.202005942
26. Y. Zhang, B. Wu, Y. He, W. Deng, J. Li et al., Layer-by-layer processed binary all-polymer solar cells with efficiency over 16% enabled by finely optimized morphology. Nano Energy **93**, 106858 (2022). https://doi.org/10.1016/j.nanoen.2021.106858
27. J. Jia, Q. Huang, T. Jia, K. Zhang, J. Zhang et al., Fine-tuning batch factors of polymer acceptors enables a binary all-polymer solar cell with high efficiency of 16.11%. Adv. Energy Mater. **12**(3), 2103193 (2022). https://doi.org/10.1002/aenm.202103193
28. H. Sun, H. Yu, Y. Shi, J. Yu, Z. Peng et al., A narrow-bandgap n-type polymer with an acceptor–acceptor backbone enabling efficient all-polymer solar cells. Adv. Mater. **32**(43), 2004183 (2020). https://doi.org/10.1002/adma.202004183
29. C. Sun, J.W. Lee, S. Seo, S. Lee, C. Wang et al., Synergistic engineering of side chains and backbone regioregularity of polymer acceptors for high-performance all-polymer solar cells with 15.1% efficiency. Adv. Energy Mater. **12**(3), 2103239 (2021). https://doi.org/10.1002/aenm.202103239
30. W. Wang, Q. Wu, R. Sun, J. Guo, Y. Wu et al., Controlling molecular mass of low-band-gap polymer acceptors for high-performance all-polymer solar cells. Joule **4**(5), 1070–1086 (2020). https://doi.org/10.1016/j.joule.2020.03.019
31. F. Peng, K. An, W. Zhong, Z. Li, L. Ying et al., A universal fluorinated polymer acceptor enables all-polymer solar cells with >15% efficiency. ACS Energy Lett. **5**(12), 3702–3707 (2020). https://doi.org/10.1021/acsenergylett.0c02053
32. C. Lee, S. Lee, G.U. Kim, W. Lee, B.J. Kim, Recent advances, design guidelines, and prospects of all-polymer solar cells. Chem. Rev. **119**(13), 8028–8086 (2019). https://doi.org/10.1021/acs.chemrev.9b00044
33. J.W. Lee, B.S. Ma, J. Choi, J. Lee, S. Lee et al., Origin of the high donor–acceptor composition tolerance in device performance and mechanical robustness of all-polymer solar cells. Chem. Mater. **32**(1), 582–594 (2020). https://doi.org/10.1021/acs.chemmater.9b04464
34. Z. Genene, J.W. Lee, S.W. Lee, Q. Chen, Z. Tan et al., Polymer acceptors with flexible spacers afford efficient and mechanically robust all-polymer solar cells. Adv. Mater. **34**(6), 2107361 (2020). https://doi.org/10.1002/adma.202107361
35. J.W. Lee, D. Jeong, D.J. Kim, T.N.L. Phan, J.S. Park et al., Flexible-spacer incorporated polymer donors enable superior blend miscibility for high-performance and mechanically-robust polymer solar cells. Energy Environ. Sci. **14**(7), 4067–4076 (2021). https://doi.org/10.1039/D1EE01062J
36. N. Kazerouni, E.L. Melenbrink, P. Das, B.C. Thompson, Ternary blend organic solar cells incorporating ductile conjugated polymers with conjugation break spacers. ACS Appl. Polym. Mater. **3**(6), 3028–3037 (2021). https://doi.org/10.1021/acsapm.1c00213
37. B.C. Schroeder, Y.C. Chiu, X. Gu, Y. Zhou, J. Xu et al., Non-conjugated flexible linkers in semiconducting polymers: a pathway to improved processability without compromising device performance. Adv. Electron. Mater. **2**(7), 1600104 (2016). https://doi.org/10.1002/aelm.201600104
38. Q. Fan, R. Ma, T. Liu, J. Yu, Y. Xiao et al., High-performance all-polymer solar cells enabled by a novel low bandgap non-fully conjugated polymer acceptor. Sci. China Chem. **64**(8), 1380–1388 (2021). https://doi.org/10.1007/s11426-021-1020-7
39. Q. Fan, W. Su, S. Chen, T. Liu, W. Zhuang et al., A non-conjugated polymer acceptor for efficient and thermally stable all-polymer solar cells. Angew. Chem. Int. Ed. **59**(45), 19835–19840 (2020). https://doi.org/10.1002/anie.202005662
40. W. Su, Q. Fan, I. Jalan, Y. Wang, W. Peng et al., Non-conjugated terpolymer acceptors with two different fused-ring electron-deficient building blocks for efficient all-polymer solar cells. ACS Appl. Mater. Interfaces **13**(5), 6442–6449 (2021). https://doi.org/10.1021/acsami.0c17722
41. Y. Liu, X.Y. Wang, Z.Y. Wang, Y. Lu, X.F. Cheng et al., Systematically investigating the effect of the aggregation behaviors in solution on the charge transport properties of BDOPV-based polymers with conjugation-break spacers. Polym. Chem. **12**(3), 370–378 (2021). https://doi.org/10.1039/D0PY01491E
42. W.W. McNutt, A. Gumyusenge, L.A. Galuska, Z. Qian, J. He et al., N-type complementary semiconducting polymer blends. ACS Appl. Polym. Mater. **2**(7), 2644–2650 (2020). https://doi.org/10.1021/acsapm.0c00261
43. L.A. Galuska, W.W. McNutt, Z. Qian, S. Zhang, D.W. Weller et al., Impact of backbone rigidity on the thermomechanical properties of semiconducting polymers with conjugation break spacers. Macromolecules **53**(14), 6032–6042 (2020). https://doi.org/10.1021/acs.macromol.0c00889
44. J. Mun, G.J.N. Wang, J.Y. Oh, T. Katsumata, F.L. Lee et al., Effect of nonconjugated spacers on mechanical properties of semiconducting polymers for stretchable transistors. Adv.

Func. Mater. **28**(43), 1804222 (2018). https://doi.org/10.1002/adfm.201804222

45. X. Zhao, Y. Zhao, Q. Ge, K. Butrouna, Y. Diao et al., Complementary semiconducting polymer blends: the influence of conjugation-break spacer length in matrix polymers. Macromolecules **49**(7), 2601–2608 (2016). https://doi.org/10.1021/acs.macromol.6b00050
46. Z. Du, X. Bao, Y. Li, D. Liu, J. Wang et al., Balancing high open circuit voltage over 1.0V and high short circuit current in benzodithiophene-based polymer solar cells with low energy loss: a synergistic effect of fluorination and alkylthiolation. Adv. Energy Mater. **8**(8), 1701471 (2018). https://doi.org/10.1002/aenm.201701471
47. F. Yang, C. Li, W. Lai, A. Zhang, H. Huang et al., Halogenated conjugated molecules for ambipolar field-effect transistors and non-fullerene organic solar cells. Mater. Chem. Front. **1**(7), 1389–1395 (2017). https://doi.org/10.1039/C7QM00025A
48. Z. Zheng, H. Yao, L. Ye, Y. Xu, S. Zhang et al., PBDB-T and its derivatives: a family of polymer donors enables over 17% efficiency in organic photovoltaics. Mater. Today **35**, 115–130 (2020). https://doi.org/10.1016/j.mattod.2019.10.023
49. Q.Y. Li, Z.F. Yao, J.Y. Wang, J. Pei, Multi-level aggregation of conjugated small molecules and polymers: from morphology control to physical insights. Rep. Prog. Phys. **84**(7), 076601 (2021). https://doi.org/10.1088/1361-6633/abfaad
50. S. Seo, J. Kim, H. Kang, J.W. Lee, S. Lee et al., Polymer donors with temperature-insensitive, strong aggregation properties enabling additive-free, processing temperature-tolerant high-performance all-polymer solar cells. Macromolecules **54**(1), 53–63 (2021). https://doi.org/10.1021/acs.macromol.0c02496
51. N. Wang, Y. Yu, R. Zhao, Z. Ding, J. Liu et al., Improving active layer morphology of all-polymer solar cells by solution temperature. Macromolecules **53**(9), 3325–3331 (2020). https://doi.org/10.1021/acs.macromol.0c00633
52. N. Wang, X. Long, Z. Ding, J. Feng, B. Lin et al., Improving active l ayer morphology of all-polymer solar cells by dissolving the two polymers individually. Macromolecules **52**(6), 2402–2410 (2019). https://doi.org/10.1021/acs.macromol.9b00057
53. T. Jia, J. Zhang, W. Zhong, Y. Liang, K. Zhang et al., 14.4% efficiency all-polymer solar cell with broad absorption and low energy loss enabled by a novel polymer acceptor. Nano Energy **72**, 104718 (2020). https://doi.org/10.1016/j.nanoen.2020.104718
54. L. Zhang, T. Jia, L. Pan, B. Wu, Z. Wang et al., 15.4% efficiency all-polymer solar cells. Sci. China Chem. **64**(3), 408–412 (2021). https://doi.org/10.1007/s11426-020-9935-2
55. S.R. Cowan, A. Roy, A.J. Heeger, Recombination in polymer-fullerene bulk heterojunction solar cells. Phys Rev. B **82**(24), 245207 (2010). https://doi.org/10.1103/PhysRevB.82.245207
56. L.J.A. Koster, M. Kemerink, M.M. Wienk, K. Maturová, R.A. Janssen, Quantifying bimolecular recombination losses in organic bulk heterojunction solar cells. Adv. Mater. **23**(14), 1670–1674 (2011). https://doi.org/10.1002/adma.201004311
57. J.H. Kim, A. Nizami, Y. Hwangbo, B. Jang, H.J. Lee et al., Tensile testing of ultra-thin films on water surface. Nat. Commun. **4**, 2520 (2013). https://doi.org/10.1038/ncomms3520
58. T. Kim, J.H. Kim, T.E. Kang, C. Lee, H. Kang et al., Flexible, highly efficient all-polymer solar cells. Nat. Commun. **6**, 8547 (2015). https://doi.org/10.1038/ncomms9547
59. S. Mukherjee, C.M. Proctor, G.C. Bazan, T.Q. Nguyen, H. Ade, Significance of average domain purity and mixed domains on the photovoltaic performance of high-efficiency solution-processed small-molecule BHJ solar cells. Adv. Energy Mater. **5**(21), 1500877 (2015). https://doi.org/10.1002/aenm.201500877
60. L. Ye, X.C. Jiao, M. Zhou, S.Q. Zhang, H.F. Yao et al., Manipulating aggregation and molecular orientation in all-polymer photovoltaic cells. Adv. Mater. **27**(39), 6046–6054 (2015). https://doi.org/10.1002/adma.201503218
61. J.W. Lee, B.S. Ma, H.J. Kim, T.S. Kim, B.J. Kim, High-molecular-weight electroactive polymer additives for simultaneous enhancement of photovoltaic efficiency and mechanical robustness in high-performance polymer solar cells. JACS Au **1**(5), 612–622 (2021). https://doi.org/10.1021/jacsau.1c00064
62. L. Ye, H.W. Hu, M. Ghasemi, T. Wang, B.A. Collins et al., Quantitative relations between interaction parameter, miscibility and function in organic solar cells. Nat. Mater. **17**(3), 253–260 (2018). https://doi.org/10.1038/s41563-017-0005-1
63. K.H. Kim, H. Kang, S.Y. Nam, J. Jung, P.S. Kim et al., Facile synthesis of o-xylenyl fullerene multiadducts for high open circuit voltage and efficient polymer solar cells. Chem. Mater. **23**(22), 5090–5095 (2011). https://doi.org/10.1021/cm202885s

 https://doi.org/10.1007/s40820-022-00884-8